Perovskite-WS$_2$ Nanosheet Composite Optical Absorbers on Graphene as High-Performance Phototransistors

Dan-Dan Zhang[1] and Rong-Mei Yu[2]*

[1] *Jiangsu Key Laboratory for Carbon-Based Functional Materials and Devices, Institute of Functional Nano and Soft Materials (FUNSOM), Soochow University, Suzhou, China,* [2] *College of Physics and Electronic Engineering, Nanyang Normal University, Nanyang, China*

High-responsivity phototransistors with a structure of perovskite-WS$_2$ nanosheet composite optical absorber and a reduced graphene oxide (rGO) channel layer is demonstrated via a facile and low-cost solution-processing method. The WS$_2$ nanosheets are dispersed within the perovskite matrix, forming the perovskite-WS$_2$ bulk heterojunction (BHJ). The hybrid phototransistor exhibits excellent figures of merit including high photoresponsivity of 678.8 A/W, high specific detectivity of 4.99×10^{11} Jones, high EQE value of 2.04×10^5% and rapid response to photoswitching. The high photoresponsivity could be attributed to the WS$_2$ nanosheets induced photo-generated electron-hole separation promotion effects due to the selective electron trapping effects in the WS$_2$ nanosheets, together with the high carrier mobility of the rGO channel. This work provides a promising platform for constructing high-responsivity photodetectors.

Keywords: reduced graphene oxide, perovskite, WS$_2$, bulk heterojunction, photodetection

INTRODUCTION

Graphene has attracted extensive interests for photodetection owing to its ultrahigh carrier mobility and wavelength independent broadband light absorption (Novoselov et al., 2005; Qiao et al., 2015; Han et al., 2019). Impressive progresses have been made in graphene-based photodetectors as promising candidates to replace traditional silicon-based photodetectors. However, the ~2.3% incident light absorption of intrinsic single-layer graphene prevented efficient photocarrier generation or accumulation, resulting in low responsivity and photoconductive gain (Xia et al., 2009; Zhang et al., 2013; Yu et al., 2017). Hybridization of graphene with photosensitizer has been proved to be an effective approach to obtain high-responsivity graphene based photodetectors (Konstantatos et al., 2012; Lee et al., 2014; Xu et al., 2014; Bessonov et al., 2017; Ni et al., 2017). This graphene/photosensitizer heterostructure exhibits the superior light absorption and high charge mobility for achieving high-responsivity photodetectors. In the field-effect transistors (FETs) utilizing the graphene/photosensitizer heterostructure as channel, the photo-generated electron-hole pairs in the photosensitizer under light will be transferred to graphene. The remained carriers in the photosensitizer produces a photogating effect in graphene, and the change in the conductivity of graphene depends on the net amount of carriers in the photosensitizer. Therefore, a promising strategy for enhancing the photodetection performance is to reduce the carrier recombination within the photosensitizer and transfer one type of carriers to graphene while the other type is trapped in the photosensitizer.

Recently, organometal halide perovskite ($CH_3NH_3PbX_3$, X = I, Br, Cl) has emerged as a promising photosensitizer due to its excellent optical and electrical properties and ease of solution-processing (Liu et al., 2013; Wehrenfenning et al., 2013; Zuo et al., 2016). Combined with the high carrier mobility of graphene, perovskite/graphene heterostructures have been widely explored in perovskite/graphene field-effect transistor (perovskite/GFET) phototransistors toward high-responsivity (Lee et al., 2014; Spina et al., 2015; Wang et al., 2015; Sun et al., 2016; Bessonov et al., 2017; Qian et al., 2017; Peng et al., 2018). Tremendous efforts have also been made to promote the electron-hole separation and selective charge trapping according to the detection mechanism (Qian et al., 2017; Qin et al., 2017; Xie, 2017; Peng et al., 2018). For example, Yan et al. reported a perovskite/ P3HT/ graphene multilayer heterostructure phototransistor due to the promoted photo-generated electron-hole separation and electron trapping in the perovskite layer (Xie, 2017). Nevertheless, the photo-generated electron-hole recombination within the perovskite layer before the interfacial effects would still limit the photoresponse. Moreover, the reported perovskite/GFET devices are mainly based on mechanically exfoliated or chemically vapor deposited (CVD) single and few layered graphene (Lee et al., 2014; Spina et al., 2015; Wang et al., 2015; Sun et al., 2016; Bessonov et al., 2017), and the fabrication processes are expensive and complicated. Therefore, it is necessary to design an efficient device structure with improved performances by a cheap and convenient technique.

In this work, we demonstrate a solution-processed phototransistor with a hybrid channel consisting of perovskite/WS_2 nanosheet composite optical absorbers and reduced graphene oxide (rGO), which exhibits excellent photodetection behaviors. The WS_2 nanosheets are well-dispersed within the perovskite matrix, forming the perovskite/WS_2 nanosheet bulk heterojunction (BHJ) layer. The WS_2 nanosheets can effectively promote the photo-generated electron-hole separation within the BHJ film owing to the selective electron trapping effects in the WS_2 nanosheets, and more photo-induced holes are transferred to the rGO channel for improved photodetection. This hybrid phototransistor shows a fast photoresponse with a high photoresponsivity of 678.8 A/W, high specific detectivity of 4.99×10^{11} Jones and high EQE value of 2.04×10^5%, which are about 3.5 times enhancement compared with the perovskite-only device. The results provide an alternative strategy of constructing BHJ films as the photosensitizer toward high-performance photodetectors.

EXPERIMENTAL SECTION

Graphene oxide (GO) solution (0.5 mg/mL) and WS_2 nanosheets were obtained from Nanjing XFNANO Materials Tech. Co., Ltd. CH_3NH_3I, PbI_2, 3-aminopropyltriethoxysilane, dimethyl sulfoxide and N, N-dimethylformanide were purchased from Alfa Aesar. Toluene was purchased from Aladdin. All these materials and chemicals were used without further purification.
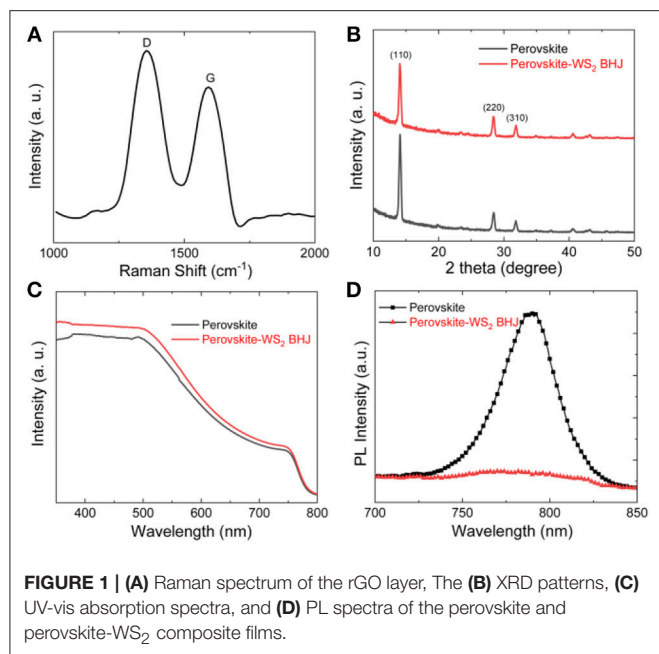
(100) oriented N-type heavily doped Si wafers with 90 nm SiO_2 layers were sequentially cleaned in acetone, anhydrous ethanol and isopropyl alcohol (IPA) for 15 min via ultrasonic treatment, followed by a 20-min UV-Ozone treatment. The cleaned SiO_2/Si substrates were soaked in a 1 vol.% APTES toluene solution for 30 min in order to assemble the APTES monolayer on the surface. Graphene oxide (GO) solution was spin-coated onto the SiO_2/Si substrates via the APTES monolayer and rinsed by DI water, followed by mild reduction into reduced GO (rGO) with a 30-min 150°C annealing treatment in air ambient. The $CH_3NH_3PbI_3$ perovskite precursor was prepared by dissolving CH_3NH_3I:PbI_2 (1 mmol:1 mmol) in 1 mL coalescing solvents of DMSO: DMF 3:7 (ν/ν) and stirring at 60 °C overnight. For the perovskite-WS_2 nanosheets composite precursor, the WS_2 nanosheets were mixed with the above $CH_3NH_3PbI_3$ solution with a concentration of 0.05 wt.%. Subsequently, for fabricating pristine $CH_3NH_3PbI_3$ and $CH_3NH_3PbI_3$-WS_2 composite photosensitizer films, the perovskite precursor solution was spin coated onto the rGO channel layer at 4,000 rpm for 40 s, during which chlorobenzene was dropped serving as the anti-solvent. The as-prepared films were annealed at 100°C for 10 min. Finally, 70 nm Au source/drain (S/D) electrodes were defined with a shadow mask and deposited by thermal evaporation. The effective detection area of the phototransistor is $30 \times 500\ \mu m^2$.

The Raman characterization of rGO films was carried out with a Raman spectrometer (WITec, 300R). The XRD patterns were measured with a PANalytical 80 equipment with Cu $K\alpha$ radiation. The UV-vis spectra were measured by using the photometer (Perkin Elmer, Lambda 750). The steady-state photoluminescence (PL) spectra were recorded on a spectrofluorometer (HORIBA Scientific, FluoroMax-4) with a 532 nm laser. The photodetection performances of the pristine and hybrid phototransistor were studied using an Agilent B1500A semiconductor analyzer in air at room temperature. The monochromic light with different wavelengths was induced by a light-emitting diode illuminant.

RESULTS AND DISCUSSION

GO sheets were firstly spin-coated onto the SiO_2/Si substrate via the monolayer APTES, and then were mildly reduced at 150°C for 30 min to obtain the rGO layer with higher electrical conductivity. **Figure 1A** shows the Raman spectrum of the rGO films with typical D and G bands at around 1,340 and 1,580 cm^{-1}, respectively. The G band could be attributed to the graphitic carbon, while the D band is related to the structural defects or partially disordered graphitic domains (Han et al., 2015; Wasalathilake et al., 2018). The I_D/I_G ratio is calculated to be 1.21, larger than the GO nanosheets, which indicates the effective reduction of GO into rGO and the partial restoration of the conjugated structures during the reduction process (Han et al., 2015; Zhu et al., 2019). Then, a one-step method was adopted to deposit the perovskite and perovskite-WS_2 BHJ film on the rGO conductive layer, followed by evaporation of Au electrodes. The WS_2 nanosheets exhibit a typical 2H phase, confirmed by the XRD patterns (**Figure S1**) (Liu et al., 2018). XRD patterns of both $CH_3NH_3PbI_3$ and $CH_3NH_3PbI_3$-WS_2

FIGURE 1 | (A) Raman spectrum of the rGO layer, The (B) XRD patterns, (C) UV-vis absorption spectra, and (D) PL spectra of the perovskite and perovskite-WS$_2$ composite films.

composite films have similar structural features (**Figure 1B**), showing three main peaks at $2\theta = 14.05°$, $28.41°$, and $31.87°$ associated with the (110), (220), and (310) planes of the perovskite crystals, respectively. This result reflects that the addition of WS$_2$ nanosheet in the composite film has negligible effect on the crystalline structure of CH$_3$NH$_3$PbI$_3$. The UV-vis absorption spectra of the perovskite and perovskite-WS$_2$ BHJ films with the WS$_2$ concentration of 0.05 wt.% is presented in **Figure 1C**. The perovskite films with and without WS$_2$ nanosheets show broad and strong light absorption in the UV-vis region with a typical absorption edge around 786 nm. Moreover, the absorption intensity and also the spectrum profile are similar for the pristine CH$_3$NH$_3$PbI$_3$ and CH$_3$NH$_3$PbI$_3$-WS$_2$ composite films, indicating that such a low concentration WS$_2$ nanosheets contribute little to the light absorption properties of perovskite films. However, although the light absorption properties are similar, the PL peak at 776 nm arising from the interband transition of perovskite exhibits different intensities for pristine CH$_3$NH$_3$PbI$_3$ and CH$_3$NH$_3$PbI$_3$-WS$_2$ composite films, as shown in the steady-state PL spectra (**Figure 1D**). A significant PL intensity quenching in the CH$_3$NH$_3$PbI$_3$-WS$_2$ composite film is observed, demonstrating that a non-radiative kinetic process rather than the radiative recombination process is induced by WS$_2$ in the perovskite. Moreover, the weak PL intensity of perovskite-WS$_2$ composite film indicates that the WS$_2$ nanosheets provide the composite film with an advantageous energy level alignment for efficient charge transfer and separation, beneficial for promoting the photo-generated hole-electron separation and thus improved photoresponse.

Figure 2A shows the device configuration of our perovskite-WS$_2$ BHJ/rGO hybrid phototransistor. Upon illumination, electron and hole pairs are generated. The significant PL quenching (**Figure 1B**) demonstrates that the CH$_3$NH$_3$PbI$_3$-WS$_2$ bulk heterojunction (BHJ) can effectively separate the
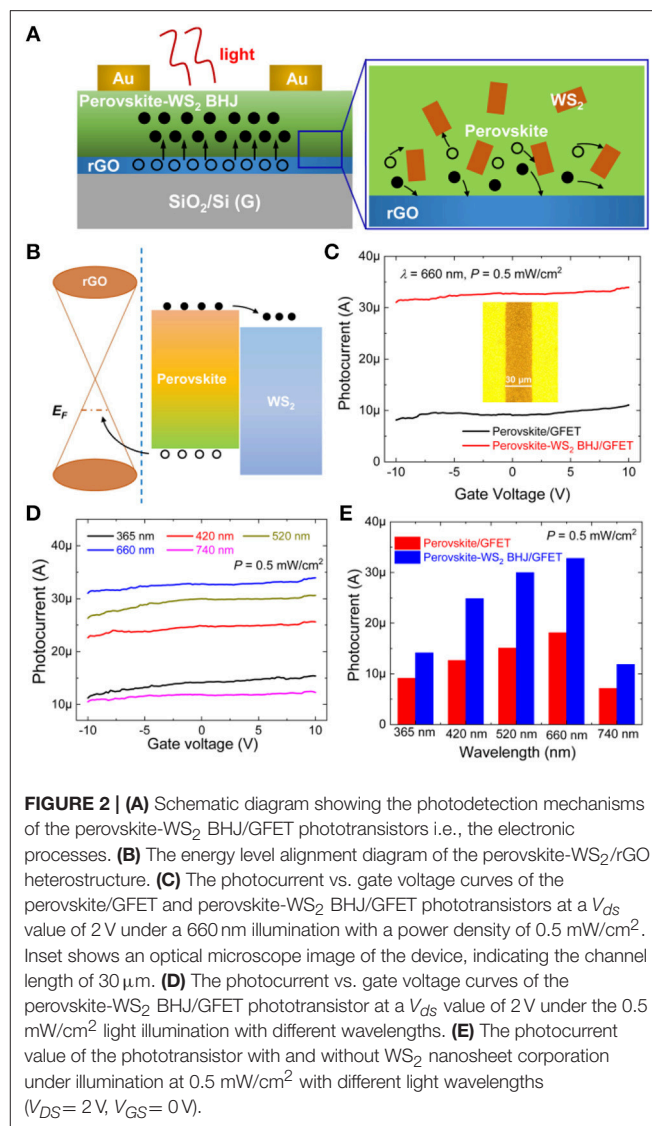
FIGURE 2 | (A) Schematic diagram showing the photodetection mechanisms of the perovskite-WS$_2$ BHJ/GFET phototransistors i.e., the electronic processes. (B) The energy level alignment diagram of the perovskite-WS$_2$/rGO heterostructure. (C) The photocurrent vs. gate voltage curves of the perovskite/GFET and perovskite-WS$_2$ BHJ/GFET phototransistors at a V_{ds} value of 2 V under a 660 nm illumination with a power density of 0.5 mW/cm^2. Inset shows an optical microscope image of the device, indicating the channel length of 30 μm. (D) The photocurrent vs. gate voltage curves of the perovskite-WS$_2$ BHJ/GFET phototransistor at a V_{ds} value of 2 V under the 0.5 mW/cm^2 light illumination with different wavelengths. (E) The photocurrent value of the phototransistor with and without WS$_2$ nanosheet corporation under illumination at 0.5 mW/cm^2 with different light wavelengths ($V_{DS} = 2$ V, $V_{GS} = 0$ V).

photo-generated holes and electrons, and the electrons are transferred to WS$_2$, resulting in the significant suppression of the electron-hole recombination in the perovskite. Moreover, as photo-generated electrons are trapped in the BHJ film, only holes are transferred to the rGO channel owing to the energy barrier between the perovskite and rGO film. Therefore, more negative charges will build up in the CH$_3$NH$_3$PbI$_3$-WS$_2$ BHJ photosensitizer layer, and this will induce more hole doping in rGO, which improves the photoresponse properties. The energy level alignment diagram of the perovskite-WS$_2$ BHJ/rGO hybrid device structure and the corresponding electronic processes are depicted in **Figure 2B** according to the reported energy levels of perovskite, WS$_2$ and graphene (Ma et al., 2016; Zhang et al., 2017). As a result of different Fermi levels and energy levels of CH$_3$NH$_3$PbI$_3$ and WS$_2$, photo generated electrons are transferred to WS$_2$ and then holes and electrons are separated, which reduces the charge recombination within perovskite and thus enhances the photodetection performances.

To demonstrate the hole doping effects in rGO, the transfer curve of the phototransistor with and without WS$_2$ nanosheets at $V_{ds} = 2$ V is measured in dark and upon illumination of monochromic light with different wavelengths (365, 420, 520, 660, and 740 nm) and light intensities. **Figure 2C** shows the photocurrent vs. gate voltage curves of the perovskite/GFET and perovskite-WS$_2$ BHJ/GFET phototransistors under light illumination ($\lambda = 660$ nm, $P = 0.5$ mW/cm^2). Inset of **Figure 2C** exhibits the optical microscope image of the device, and it can be clearly seen that the channel length is measured to be 30 μm. Here, the photocurrent is defined as the difference between the current under light illumination and dark conditions. The photocurrent can be modulated efficiently by altering the gate voltage, indicating the gate modulation effects on the photoresponse behaviors. Moreover, the hybrid perovskite-WS$_2$ BHJ/ GFET device shows a greatly enhanced photocurrent value at V_{GS} ranging from -10 to 10 V compared with the perovskite-only device, confirming the roles of perovskite-WS$_2$ BHJ on promoting the electron-hole separation and electron trapping effects. Especially, at $V_{DS} = 2$ V and $V_{GS} = 0$ V, the photocurrent of the perovskite-WS$_2$ BHJ/GFET phototransistor is 32.79 μA, almost 3.5 times of that of the perovskite/GFET phototransistor (9.06 μA). This high photocurrent value is attributed to the electron-hole separation promotion effects of the CH$_3$NH$_3$PbI$_3$-WS$_2$ BHJ, high optical absorption and light-to-electron conversion efficiency of perovskite and the high carrier mobility of rGO channel layer. **Figure 2D** presents the wavelength dependence of the photocurrent vs. gate voltage characteristics in the perovskite-WS$_2$ BHJ/GFET phototransistor at $P = 0.5$ mW/cm^2 and $V_{DS} = 2.0$ V. The hybrid phototransistor exhibits different photoresponse behaviors to monochromic light illumination with different wavelengths i.e., the maximum photocurrent can be obtained under 660 nm wavelength and decreases under light illumination with longer and shorter wavelengths. The decrease of photocurrent at long wavelengths is attributed to the reduced long-wavelength light absorption of perovskite as shown in **Figure 1C**, while the photocurrent decrease at short wavelengths is possibly due to the low light-to-photon conversion efficiency of perovskite at short wavelengths. Moreover, it can also be seen that the gate modulation effects on photocurrent can be observed under illumination with all wavelengths (365, 420, 520, 660, and 740 nm). The photocurrents of the pristine perovskite/GFET and composite perovskite-WS$_2$ BHJ/GFET devices under light illumination with different light wavelengths and the same power density (0.5 mW/cm^2) are extracted and shown in **Figure 2E**. Compared with the pristine perovskite/GFET phototransistor, the photocurrents are greatly increased at all the wavelengths upon the addition of such a low concentration WS$_2$ nanosheets. Especially, the photocurrents under the visible light illumination (420, 520, and 660 nm) increase more obviously than the light illumination cases with other UV and NIR wavelengths, indicating the photoresponse enhancement should be attributed to the perovskite-WS$_2$ BHJ effect rather than the light absorption enhancement in the perovskite-WS$_2$ BHJ/GFET phototransistor.

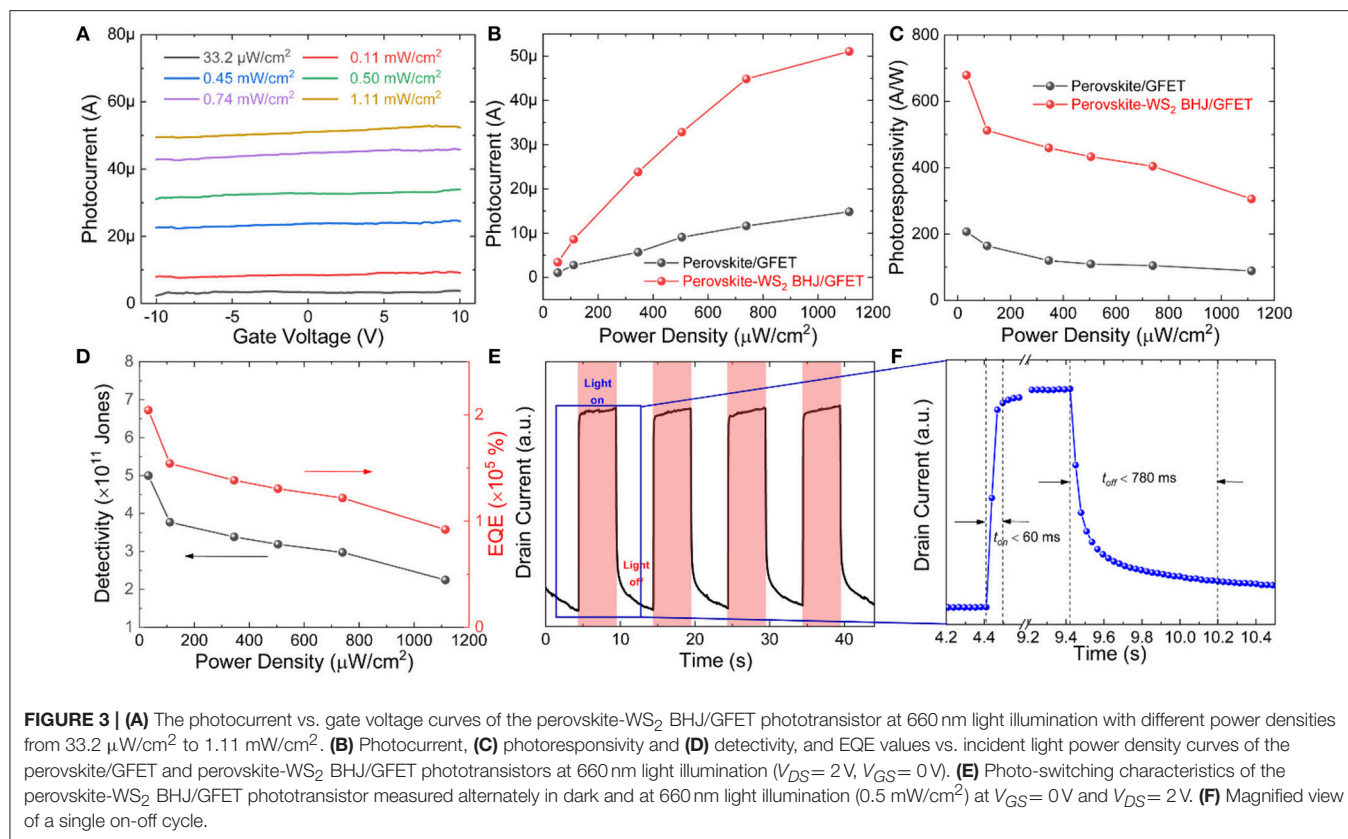The light power dependences of the photoresponse behavior in the perovskite-WS$_2$ BHJ/GFET phototransistor are further characterized. **Figure 3A** shows the photocurrent vs. gate voltage curves of the perovskite-WS$_2$ BHJ/GFET phototransistor at 660 nm light illumination with power densities from 33.2 μW/cm^2 to 1.11 mW/cm^2. It can also be observed that the photocurrent could be modulated efficiently by the gate voltage, and the dependence of the photocurrent on the gate voltage increases at higher incident light power density. The extracted photocurrent value at $V_{DS} = 2$ V and $V_{GS} = 0$ V increases linearly with the increase of the incident light power density at the low power density region, and then becomes saturated in the high light power density region owing to the increased photo-excited carrier recombination rate (**Figure 3B**). Besides, the photoresponsivity decreases greatly with increasing the incident light power density (**Figure 3C**). Significantly, the photodetection performances of the perovskite-WS$_2$ BHJ/GFET phototransistor including photocurrent and photoresponsivity are much superior to that of the perovskite/GFET phototransistor, demonstrating the key role of the perovskite-WS$_2$ BHJ on photoresponse enhancement. At $V_{DS} = 2$ V and $V_{GS} = 0$ V, a high photoresponsivity of 678.8 A/W at an incident power density of 33.2 μW/cm^2 is achieved in the perovskite-WS$_2$ BHJ/GFET phototransistor, which is about 3 times larger than that of the pristine perovskite/GFET phototransistor (207 A/W). Even higher photoresponsivity could be achieved if the incident light with lower power density or a larger bias voltage is adopted, however, this high photoresponsivity performance is high enough for the practical applications. Moreover, it should also be noted that such high photoresponsivity is achieved at such a low operation voltage ($V_{DS} = 2$ V and $V_{GS} = 0$ V), which makes it more promising for practical applications.

To further evaluate the photodetection performances of the phototransistor, other important figures of merits such as specific detectivity and external quantum efficiency (EQE) are also calculated. The specific detectivity (D^*) enables the device performance comparison between photodetectors with different device geometries and photosensitive areas. The shot noise is assumed to be mainly from the contribution of dark current and thus the specific detectivity can be calculated according to the following formula:

$$D^* = \frac{R(A)^{1/2}}{(2qI_{dark})^{1/2}}$$

where R is the photoresponsivity, A is the photosensitive area, q is the electric charge and I_{dark} is the dark current. The calculated detectivity vs. power density curve is depicted in **Figure 3D**, and the detectivity shows similar dependence on power density as photoresponsivity. The maximum D^* value at an incident power density of 33.2 μW/cm^2 is calculated to be 4.99×10^{11} Jones, which is comparable with commercial Si photodiodes ($\sim 4 \times 10^{12}$ Jones) (Gong et al., 2009). Besides, EQE is also calculated using the following formula:

$$EQE = \frac{Rhc}{\lambda q}$$

FIGURE 3 | (A) The photocurrent vs. gate voltage curves of the perovskite-WS$_2$ BHJ/GFET phototransistor at 660 nm light illumination with different power densities from 33.2 μW/cm^2 to 1.11 mW/cm^2. **(B)** Photocurrent, **(C)** photoresponsivity and **(D)** detectivity, and EQE values vs. incident light power density curves of the perovskite/GFET and perovskite-WS$_2$ BHJ/GFET phototransistors at 660 nm light illumination (V_{DS} = 2 V, V_{GS} = 0 V). **(E)** Photo-switching characteristics of the perovskite-WS$_2$ BHJ/GFET phototransistor measured alternately in dark and at 660 nm light illumination (0.5 mW/cm^2) at V_{GS} = 0 V and V_{DS} = 2 V. **(F)** Magnified view of a single on-off cycle.

where hc/λ represents the photon energy, R is the photoresponsivity and q is the electric charge. The calculated EQE vs. light power density value is presented in **Figure 3D**, and it is clearly seen that the EQE value also increases with decreasing the light power density. Notably, the perovskite-WS$_2$/GFET phototransistor also exhibits much higher *EQE* values than the pristine perovskite/GFET phototransistor, and the highest EQE reaches a remarkable value as high as 2.04×10^5%.

Except for the above photoresponse parameters, the photoresponse speed is also an important parameter for photodetectors. **Figure 3E** shows the temporal photocurrent response of the perovskite-WS$_2$ BHJ/GFET phototransistor upon illumination with a 0.5 mW/cm^2 660 nm light at V_{DS} = 2 V and V_{GS} = 0 V. The light on/off time interval is set as 5 s. The phototransistor exhibits highly stable and reproducible photoresponse behaviors. The rise or fall time was measured to be <60 or 780 ms (**Figure 3F**), revealing its relatively fast photoresponse rate. However, a slower decay process is observed when the light is turned off, which is possibly due to the trapping effects of the interface states or film defects on the photo-generated carriers.

CONCLUSIONS

In conclusions, the perovskite-WS$_2$ nanosheet composite optical absorber was deposited on reduced graphene oxide to construct high-responsivity perovskite-WS$_2$/rGO phototransistors via a facile and cheap solution-processing strategy. The

WS$_2$ nanosheets are well-dispersed within the perovskite matrix by a mixed perovskite-WS$_2$ precursor, forming the perovskite-WS2 bulk heterojunction. The hybrid phototransistor shows outstanding photoresponse behaviors including high responsivity of 678.8 A/W, high specific detectivity of 4.99×10^{11} Jones and ultrahigh EQE value of 2.04×10^5%, which is about 3.5 times of those of the perovskite/GFET phototransistor without WS$_2$ nanosheets. Moreover, it also exhibits excellent photoresponse-irradiance dependence characteristics and rapid response to photoswitching. The excellent photodetection behaviors of the hybrid phototransistor is attributed to the WS$_2$ nanosheets induced photo-generated electron-hole separation promotion effects due to the selective electron trapping effects in the WS$_2$ nanosheets, together with the high carrier mobility of the rGO channel. The solution-processing fabrication method along with its outstanding photoresponse behaviors makes the perovskite-WS$_2$ BHJ/GFET phototransistor promising for future practical photodetection applications.

AUTHOR CONTRIBUTIONS

R-MY designed the experiments. D-DZ conducted the experiments, analyzed the data and wrote the manuscript.

ACKNOWLEDGMENTS

SUPPLEMENTARY MATERIAL

REFERENCES

Bessonov, A. A., Allen, M., Liu, Y., Malik, S., Bottomley, J., Rushton, A., et al. (2017). Compound quantum dot-perovskite optical absorbers on graphene enhancing short-wave infrared photodetection. *ACS Nano* 11, 5547–5557. doi: 10.1021/acsnano.7b00760

Gong, X., Tong, M. H., Xia, Y. J., Cai, W. Z., Moon, J. S., Cao, Y., et al. (2009). High-detectivity polymer photodetectors with spectral response from 300 nm to 1450 nm. *Science* 325, 1665–1667. doi: 10.1126/science.1176706

Han, B., Zhang, Y. L., Zhu, L., Li, Y., Ma, Z. C., Liu, Y. Q., et al. (2019). Plasmonic-assisted graphene oxide muscles. *Adv. Mater.* 31:1806386. doi: 10.1002/adma.201806386

Han, D., Zhang, Y. L., Jiang, H. B., Xia, H., Feng, J., Chen, Q. D., et al. (2015). Moisture-responsive graphene paper prepared by self-controlled photoreduction. *Adv. Mater.* 27, 332–338. doi: 10.1002/adma.201403587

Konstantatos, G., Badioli, M., Gaudreau, L., Osmond, J., Bernechea, M., Arquer, F., et al. (2012). Hybrid graphene-quantum dot phototransistors with ultrahigh gain. *Nat. Nanotech.* 7, 363–368. doi: 10.1038/nnano.2012.60

Lee, Y. B., Kwon, J., Hwang, E., Ra, C., Yoo, W. J., Ahn, J. H., et al. (2014). High-performance perovskite-graphene hybrid photodetector. *Adv. Mater.* 27, 41–46. doi: 10.1002/adma.201402271

Liu, M. Z., Johnston, M. B., and Snaith, H. J. (2013). Efficient pla nar heterojunction perovskite solar cells by vapor deposition. *Nature* 501, 395–398. doi: 10.1038/nature12509

Liu, Z. Q., Li, N., Su, C., Zhao, H. Y., Xu, L. L., Yin, Z. Y., et al. (2018). Colloidal synthesis of 1T' phase dominated WS2 toward endurable electrocatalysis. *Nano Energy* 50, 176–181. doi: 10.1016/j.nanoen.2018.05.019

Ma, C., Shi, Y. M., Hu, W. J., Chiu, M. H., Liu, Z. X., Bera, A., et al. (2016). Heterostructured WS2/CH3NH3PbI3 photoconductors with suppressed dark current and enhanced photodetectivity. *Adv. Mater.* 28, 3683–3689. doi: 10.1002/adma.201600069

Ni, Z. Y., Ma, L. L., Du, S. C., Xu, Y., Yuan, M., Fang, H. H., et al. (2017). Plasmonic silicon quantum dots enables high-sensitivity ultrabroadband photodetection of graphene-based hybrid phototransistors. *ACS Nano* 11, 9854–9862. doi: 10.1021/acsnano.7b03569

Novoselov, K. S., Geim, A. K., Morozov, S. V., Jiang, D., Katsnel son, M. I., Grigorieva, I. V., et al. (2005). Two-dimensional gas of massless dirac fermions in graphene. *Nature* 438, 197–200. doi: 10.1038/nature04233

Peng, Z. Y., Xu, J. L., Zhang, J. Y., Gao, X., and Wang, S. D. (2018). Solution-processed high-performance hybrid photodetectors enhanced by perovskite/MoS2 bulk heterojunction. *Adv. Mater. Interfaces* 5:1800505. doi: 10.1002/admi.201800505

Qian, L., Sun, Y. L., Wu, M. M., Xie, D., Ding, L., and Shi, G. Q. (2017). A solution-processed high-performance phototransistor based on a perovskite composite with chemically modified graphenes. *Adv. Mater.* 29, 1606175. doi: 10.1002/adma.201606175

Qiao, H., Yuan, J., Xu, Z. Q., Chen, C. Y., Lin, S. H., Wang, Y. S., et al. (2015). Broadband photodetectors based on graphene-Bi2Te3 heterostructure. *ACS Nano* 9, 1886–1894. doi: 10.1021/nn506920z

Qin, L., Wu, L. P., Kattel, B., Li, C., Zhang, Y., Hou, Y. B., et al. (2017). Using bulk heterojunctions and selective electron trapping to enhance the responsivity of perovskite-graphene photodetectors. *Adv. Funct. Mater.* 27:1704173. doi: 10.1002/adfm.201704173

Spina, M., Lehmann, M., Nafradi, B., Bernard, L., Bonvin, E., Gaal, R., et al. (2015). Microengineered CH3NH3PbI3 nanowire/graphene phototransistor for low-intensity light detection at room temperature. *Small* 11, 4824–4828. doi: 10.1002/amll.201501257

Sun, Z. H., Aigouy, L., and Chen, Z. Y. (2016). Plasmonic-enhanced perovskite-graphene hybrid photodetectors. *Nanoscale* 8, 7377–7385. doi: 10.1039/C5NR08677A

Wang, Y. S., Zhang, Y. P., Lu, Y., Xu, W. D., Mu, H. R., Chen, C. Y., et al. (2015). Hybrid graphene-perovskite phototransistors with ultrahigh responsivity and gain. *Adv. Opt. Mater.* 3, 1389–1396. doi: 10.1002/adom.201500150

Wasalathilake, K. C., Galpaya, D. G. D., Ayoko, G. A., and Yan, C. (2018). Understanding the structure-property relationships in hydrothermally reduced graphene oxide hydrogels. *Carbon* 137, 282–290. doi: 10.1016/j.carbon.2018.05.036

Wehrenfenning, C., Eperon, G. E., Johnston, M. B., Snaith, H. J., and Herz, L. M. (2013). High charge carrier mobilities and lifetimes in organolead trihalide perovskites. *Adv. Mater.* 26, 1584–1589. doi: 10.1002/adma.201305172

Xia, F. N., Mueller, T., Lin, Y. M., Garcia, A. V., and Avouris, P. (2009). Ultrafast graphene photodetector. *Nat. Nanotech.* 4, 839–843. doi: 10.1038/nnano.2009.292

Xie, C. (2017). Perovskite/poly(3-hexylthiophene) /graphene multiheterojunction phototransistors with ultrahigh gain in broadband wavelength region. *ACS Appl. Mater. Interfaces* 9, 1569–1576. doi: 10.1021/acsami.6b11631

Xu, H., Wu, J. X., Feng, Q. L., Mao, N. N., Wang, C. M., and Zhang, J. (2014). High responsivity and gate tunable graphene-MoS2 hybrid phototransistor. *Small* 10, 2300–2306. doi: 10.1002/smll.201303670

Yu, W. Z., Li, S. J., Zhang, Y. P., Ma, W. L., Sun, T., Yuan, J., et al. (2017). Near-infrared photodetectors based on MoTe2/graphene heterostructure with high responsivity and flexibility. *Small* 13:1700268. doi: 10.1002/smll.201700268

Zhang, C., Geng, X. P., Tang, S. L., Deng, M. S., and Du, Y. W. (2017). NiCo2O4@rGO hybrid nanostructures on Ni foam as high-performance supercapacitor electrodes. *J. Mater. Chem. A* 5, 5912–5919. doi: 10.1039/C7TA00571G

Zhang, Y. Z., Liu, T., Meng, B., Li, X. H., Liang, G. Z., Hu, X. N., et al. (2013). Broadband high photoresponse from pure monolayer graphene photodetector. *Nat. Commun.* 4:1811. doi: 10.1038/ncomms2830

Zhu, L., Gao, Y. Y., Han, B., Zhang, Y. L., and Sun, H. B. (2019). Laser fabrication of graphene-based electrothermal actuators enabling predicable deformation. *Opt. Lett.* 44, 1363–1366. doi: 10.1364/OL.44.001363

Zuo, C., Bolink, H. J., Han, H. W., Huang, J. S., Cahen, D., and Ding, L. (2016). Advances in perovskite solar cells. *Adv. Sci.* 3:1500324. doi: 10.1002/advs.201500324